Monthly Notices of the ROYAL ASTRONOMICAL SOCIETY
LETTERS

Mon. Not. R. Astron. Soc. **409,** L7–L12 (2010) doi:10.1111/j.1745-3933.2010.00950.x

HerMES: *Herschel*-SPIRE observations of Lyman break galaxies

D. Rigopoulou,[1,2][⋆] G. Magdis,[3] R. J. Ivison,[4,5] A. Amblard,[6] V. Arumugam,[5] H. Aussel,[3] A. Blain,[7] J. Bock,[7,8] A. Boselli,[9] V. Buat,[9] D. Burgarella,[9] N. Castro-Rodríguez,[10,11] A. Cava,[10,11] P. Chanial,[12] D. L. Clements,[12] A. Conley,[13] L. Conversi,[14] A. Cooray,[6,7] C. D. Dowell,[7,8] E. Dwek,[15] S. Eales,[16] D. Elbaz,[3] D. Farrah,[17] A. Franceschini,[18] J. Glenn,[13] M. Griffin,[16] M. Halpern,[19] E. Hatziminaoglou,[20] J.-S. Huang,[21] E. Ibar,[4] K. Isaak,[16] G. Lagache,[22] L. Levenson,[7,8] N. Lu,[7,23] S. Madden,[3] B. Maffei,[24] G. Mainetti,[18] L. Marchetti,[18] H. T. Nguyen,[7,8] B. O'Halloran,[12] S. J. Oliver,[17] A. Omont,[25] M. J. Page,[26] P. Panuzzo,[3] A. Papageorgiou,[16] C. P. Pearson,[1,27] I. Pérez-Fournon,[10,11] M. Pohlen,[16] D. Rizzo,[12] I. G. Roseboom,[17] M. Rowan-Robinson,[12] B. Schulz,[7,23] Douglas Scott,[19] N. Seymour,[26] D. L. Shupe,[7,23] A. J. Smith,[17] J. A. Stevens,[28] M. Symeonidis,[26] M. Trichas,[12] K. E. Tugwell,[26] M. Vaccari,[18] I. Valtchanov,[14] L. Vigroux,[25] L. Wang,[17] G. Wright,[4] C. K. Xu[7,23] and M. Zemcov[7,8]

[1] *Space Science & Technology Department, Rutherford Appleton Laboratory, Chilton, Didcot, Oxfordshire OX11 0QX*
[2] *Astrophysics, University of Oxford, Keble Road, Oxford OX1 3RH*
[3] *Laboratoire AIM-Paris-Saclay, CEA/DSM/Irfu – CNRS – Université Paris Diderot, CE-Saclay, pt courrier 131, F-91191 Gif-sur-Yvette, France*
[4] *UK Astronomy Technology Centre, Royal Observatory, Blackford Hill, Edinburgh EH9 3HJ*
[5] *Institute for Astronomy, University of Edinburgh, Royal Observatory, Blackford Hill, Edinburgh EH9 3HJ*
[6] *Department of Physics & Astronomy, University of California, Irvine, CA 92697, USA*
[7] *California Institute of Technology, 1200 E. California Blvd., Pasadena, CA 91125, USA*
[8] *Jet Propulsion Laboratory, 4800 Oak Grove Drive, Pasadena, CA 91109, USA*
[9] *Laboratoire d'Astrophysique de Marseille, OAMP, Université Aix-marseille, CNRS, 38 rue Frédéric Joliot-Curie, 13388 Marseille Cedex 13, France*
[10] *Instituto de Astrofísica de Canarias (IAC), E-38200 La Laguna, Tenerife, Spain*
[11] *Departamento de Astrofísica, Universidad de La Laguna (ULL), E-38205 La Laguna, Tenerife, Spain*
[12] *Astrophysics Group, Imperial College London, Blackett Laboratory, Prince Consort Road, London SW7 2AZ*
[13] *Department of Astrophysical and Planetary Sciences, CASA 389-UCB, University of Colorado, Boulder, CO 80309, USA*
[14] *Herschel Science Centre, European Space Astronomy Centre, Villanueva de la Cañada, 28691 Madrid, Spain*
[15] *Observational Cosmology Lab, Code 665, NASA Goddard Space Flight Center, Greenbelt, MD 20771, USA*
[16] *Cardiff School of Physics and Astronomy, Cardiff University, Queens Buildings, The Parade, Cardiff CF24 3AA*
[17] *Astronomy Centre, Department of Physics & Astronomy, University of Sussex, Brighton BN1 9QH*
[18] *Dipartimento di Astronomia, Università di Padova, vicolo Osservatorio 3, 35122 Padova, Italy*
[19] *Department of Physics & Astronomy, University of British Columbia, 6224 Agricultural Road, Vancouver, BC V6T 1Z1, Canada*
[20] *ESO, Karl-Schwarzschild-Str. 2, 85748 Garching bei München, Germany*
[21] *Harvard–Smithsonian Center for Astrophysics, MS65, 60 Garden Street, Cambridge, MA 02138, USA*
[22] *Institut d'Astrophysique Spatiale (IAS), bâtiment 121, Université Paris-Sud 11 and CNRS (UMR 8617), 91405 Orsay, France*
[23] *Infrared Processing and Analysis Center, MS 100-22, California Institute of Technology, JPL, Pasadena, CA 91125, USA*
[24] *School of Physics and Astronomy, The University of Manchester, Alan Turing Building, Oxford Road, Manchester M13 9PL*
[25] *Institut d'Astrophysique de Paris, UMR 7095, CNRS, UPMC Univ. Paris 06, 98 bis boulevard Arago, F-75014 Paris, France*
[26] *Mullard Space Science Laboratory, University College London, Holmbury St Mary, Dorking, Surrey RH5 6NT*
[27] *Institute for Space Imaging Science, University of Lethbridge, Lethbridge, Alberta T1K 3M4, Canada*
[28] *Centre for Astrophysics Research, University of Hertfordshire, College Lane, Hatfield, Hertfordshire AL10 9AB*

Accepted 2010 September 10. Received 2010 September 2; in original form 2010 June 20

[⋆] E-mail: d.rigopoulou1@physics.ox.ac.uk

ABSTRACT

We present first results of a study of the submillimetre (submm) (rest-frame far-infrared) properties of $z \sim 3$ Lyman break galaxies (LBGs) and their lower redshift counterparts BX/BM galaxies, based on *Herschel*-SPIRE observations of the Northern field of the Great Observatories Origins Deep Survey (GOODS-N). We use stacking analysis to determine the properties of LBGs well below the current limit of the survey. Although LBGs are not detected individually, stacking the infrared luminous LBGs (those detected with *Spitzer* at 24 μm) yields a statistically significant submm detection with mean flux $\langle S_{250} \rangle = 5.9 \pm 1.4$ mJy confirming the power of SPIRE in detecting UV-selected high-redshift galaxies at submm wavelengths. In comparison, the *Spitzer* 24 μm detected BX/BM galaxies appear fainter with a stacked value of $\langle S_{250} \rangle = 2.7 \pm 0.8$ mJy. By fitting the spectral energy distributions (SEDs) we derive median infrared luminosities, $L_{\rm IR}$, of 2.8×10^{12} L$_{\odot}$ and 1.5×10^{11} L$_{\odot}$ for $z \sim 3$ LBGs and BX/BMs, respectively. We find that $L_{\rm IR}$ estimates derived from present measurements are in good agreement with those based on UV data for $z \sim 2$ BX/BM galaxies, unlike the case for $z \sim 3$ infrared luminous LBGs where the UV underestimates the true $L_{\rm IR}$. Although sample selection effects may influence this result we suggest that differences in physical properties (such as morphologies, dust distribution and extent of star-forming regions) between $z \sim 3$ LBGs and $z \sim 2$ BX/BMs may also play a significant role.

Key words: galaxies: high-redshift – galaxies: starburst – submillimetre: galaxies.

1 INTRODUCTION

The broad-band dropout technique has been a very successful tool for discovering high-redshift galaxies, the so-called Lyman break galaxies (LBGs; e.g. Steidel & Hamilton 1993; Steidel et al. 1999). The initial selection focused on $z \sim 3$ samples. The same colour criteria were later extended to select LBGs at $1.4 < z < 2.5$ (the so-called BX/BM objects) with approximately the same range of UV luminosity and intrinsic UV colours as the $z \sim 3$ LBGs (Reddy et al. 2006). The dropout broad-band technique provides a complete census of UV light at high redshift, with well over a thousand galaxies detected at $z > 1.5$. Recent detailed studies including *Spitzer* observations have shown that some of these galaxies have large stellar masses $>10^{10}$ M$_{\odot}$ (e.g. Reddy et al. 2006; Rigopoulou et al. 2006; Magdis et al. 2008, 2010a) while their comoving volume density at $z \sim 3$ is $\sim$0.005 Mpc^{-3} (e.g. Reddy & Steidel 2009).

A number of issues related to the nature and properties of $z \sim 3$ LBGs remain unclear. The dust-corrected star formation rate (SFR) of LBGs can be as high as 100 M$_{\odot}$ yr^{-1}, which would correspond to $S_{850} \sim 1$ mJy depending on specific dust parameters (Chapman & Casey 2009). However, the search for the submillimetre (submm) counterparts of LBGs has proven challenging due to uncertainties in the relations used to predict the rest-frame far-infrared (FIR) luminosity from the UV. Peacock et al. (2000) analysed the submm emission from star-forming galaxies with the highest UV SFRs and found that they were statistically detected with a flux density $S_{850} = 0.2$ mJy for a SFR of $1\,h^{-2}$ M$_{\odot}$ yr^{-1}. Chapman et al. (2000) and Chapman & Casey (2009) reported the submm detection of Westphal MMD-11 and Westphal-MM8, while Rigopoulou et al. (2010) reported mm detections of a further two LBGs, EGS-D49 and EGS-M28 selected based on their strong MIPS 24 μm emission (e.g. Huang et al. 2005). Despite these promising detections the properties of the FIR and submm emission from LBGs, their dust content and their possible contribution to the cosmic FIR background is still largely unconstrained.

With the advent of *Herschel* (Pilbratt et al. 2010) it is now possible to investigate the submm (rest-frame FIR) properties of LBGs. In this Letter we report first results on the FIR properties of LBGs based on observations that are part of the *Herschel* Multi-tiered Extragalactic Survey (HerMES), a Guaranteed Time project that will eventually result in a variety of surveys of varying depth and area which will be covered in five photometric bands (110, 160, 250, 350 and 500 μm; Oliver et al. 2010). The results presented here are based on HerMES data taken as part of the *Herschel* Science Demonstration Phase. Throughout this Letter we assume $\Omega_{\rm m} = 0.3$, $\Omega_{\Lambda} = 0.72$ and $H_0 = 72\,{\rm km\,s^{-1}\,Mpc^{-1}}$.

2 OBSERVATIONS, SAMPLE SELECTION AND ANALYSIS

2.1 *Herschel* observations

Submm observations of the Northern field of the Great Observatories Origins Deep Survey (GOODS-N) were carried out at 250, 350 and 500 μm, with the Spectral and Photometric Imaging Receiver (SPIRE). The instrument and its capabilities are described in Griffin et al. (2010), while the SPIRE astronomical calibration methods and accuracy are outlined in Swinyard et al. (2010). The GOODS-N images are amongst the deepest possible with SPIRE and the instrumental noise is less than the confusion noise from overlapping faint sources. Confusion noise values of 5.8, 6.3 and 6.8 mJy beam^{-1} at 250, 350 and 500 μm, respectively, are reported in Nguyen et al. (2010). Besides blind source extraction resulting in single-band catalogues (SCAT; see Smith et al., in preparation), a novel source extraction method based on 24 μm priors has been developed to detect sources as close as possible to the confusion limit (see Roseboom et al. 2010, hereafter XID catalogue). The method uses a matrix inversion technique which relies on the assumption that sources detected in the 250 μm band will also be detected at 24 μm deep surveys (e.g. Marsden et al. 2009). The 24 μm catalogue positions are then used to find sources in the *Herschel* 250 μm images. The flux densities of the sources are allowed to vary until finally a set of flux densities is found that produce the best match to the image. In the current study we have made use of both blind (SCAT) and 24 μm prior source catalogues (XID), while for the stacking analysis we have used calibrated GOODS-N SPIRE images.

2.2 Sample selection and analysis

The GOODS-N region contains 58 UV-selected $z \sim 3$ LBGs (Steidel et al. 2003) and 212 UV-selected BX/BM objects (Reddy et al. 2006) down to $R \leq 25.5$. 49 LBGs and 200 BX/BMs have been detected with the *Spitzer* Infrared Array Camera [IRAC; down to 25.0 mag(AB) at 3.6 μm] and nine LBGs and 69 BX/BMs have also been detected with the Multi-Imager Photometer for *Spitzer* (MIPS; down to $S_{24} = 20$ μJy, 5σ). In the current study we investigate the submm properties of the UV-selected LBGs and BX/BMs focusing particularly on the sub-sample with MIPS detections: nine $z \sim 3$ LBGs and 69 $1.5 \leq z \leq 2.5$ BX/BM (hereafter the MIPS–LBG and MIPS–BX/BM samples). All LBG and BX/BM galaxies have spectroscopic redshifts determined from optical spectroscopy (Steidel et al. 2003; Reddy et al. 2006) which has also been used to confirm the absence of strong high ionization emission lines indicative of the presence of AGN. Objects classified as AGN/QSO are excluded from this study.

The LBG and BX/BM samples were matched to the blind (SCAT) and priors (XID) catalogues. An object is considered detected when its flux is at least 3σ above the noise (confusion plus instrumental). None of the LBGs and only three of the BX/BM objects are detected in the HerMES GOODS-N priors catalogue down to $S_{250} \sim 20$ mJy. We discuss the properties of individual sources in Section 2.3.

To assess the reliability of SPIRE detections at faint flux levels ($\leq$20 mJy) close to the confusion limit we first look at the flux distribution (per pixel) of the whole GOODS-N map. For the present discussion we focus on the 250 μm band which is the most sensitive and has the smallest beamsize (18 arcsec). We find that the fraction of pixels above 5, 10 and 20 mJy is 6, 4 and 0.6 per cent, respectively. These percentages imply that 16(4.5), 10(3) and 1.5(0.23) sources out of the 270(78) sources studied here could be associated with spurious detections at 5, 10 and 20 mJy. The number in parentheses correspond to the MIPS-detected objects.

Since none of the LBGs and only three of the BX/BMs are detected individually, we examine the properties of the two samples via stacking analysis. We measure flux densities directly from the calibrated GOODS-N SPIRE 250, 350 and 500 μm images (at the optical positions of the LBGs and BX/BMs). For the stacking we first consider the optically selected LBG and BX/BM samples. For the analysis we employ median stacking and stack at the optical position for each object. We exclude sources near bright objects (within 18 arcsec at 250 μm) to avoid contamination of the measured signal. Stacking the UV-selected samples returned no detections in any of the three SPIRE bands. For the LBGs we determine 3σ upper limits of $S_{250} < 2.8$ mJy, $S_{350} < 1.5$ mJy and $S_{500} < 0.9$ mJy. For the BX/BMs the corresponding (3σ) upper limits are $S_{250} < 2.02$ mJy, $S_{350} < 1.2$ mJy and $S_{500} < 0.6$ mJy, respectively.

The same stacking technique was employed to investigate the properties of the MIPS-detected LBGs and BX/BMs. In Fig. 1 we show the histograms of the 250 μm flux density distributions for the MIPS–LBGS and MIPS–BX/BMs. In the same plot, we show the normalized distribution of flux densities per pixel for the whole GOODS-N image. In both cases the distributions have positive skews and in the case of LBGs there is a clear positive tail implying that pixels containing flux from the LBGs have higher flux than the average pixel in the map. The case for the BX/BMs is not as clear. Although the BX/BM sample is bigger (69 objects versus 9) the population as a whole does not appear to strongly emit in the submm. In order to confirm that the two distributions are in fact different, we carry out a KS two-sample test. The test results, $D = 0.31$ and (probability) $\alpha(D) = 0.03$, suggest that the two flux density distributions are intrinsically different at the 2σ level. The mean flux densities are $\langle S_{250} \rangle = 5.9 \pm 1.4$ mJy (LBG) and $\langle S_{250} \rangle = 2.7 \pm 0.8$ mJy (BX/BM). The errors reported in these measurements have been quantified by stacking at nine (for the LBGs) and 69 (for the BX/BMs) random positions and then repeating the process 40 000 times. The 1σ value of the derived distribution is adopted as the uncertainty of the measurement. Stacking at 350 and 500 μm resulted in no formal detections. Instead we quote 3σ upper limits of $S_{350} < 4.9$ mJy and $S_{500} < 3.4$ mJy for the MIPS–LBGS and $S_{350} < 2.6$ mJy and $S_{500} < 1.6$ mJy for the MIPS–BX/BMs, respectively.

A likely physical explanation for this difference in detection rates comes from the mid-infrared (MIR) properties of the two samples. For $z \sim 3$ LBGs the MIPS 24 μm band contains contributions from 6 μm (hot) dust continuum plus the 6.2 μm emission from polycyclic aromatic hydrocarbons (PAHs). The PAH contribution to the MIPS 24 μm flux is ~20–30 per cent (e.g. Huang et al. 2005), therefore, the MIPS 24 μm flux mostly reflects the strength of the underlying

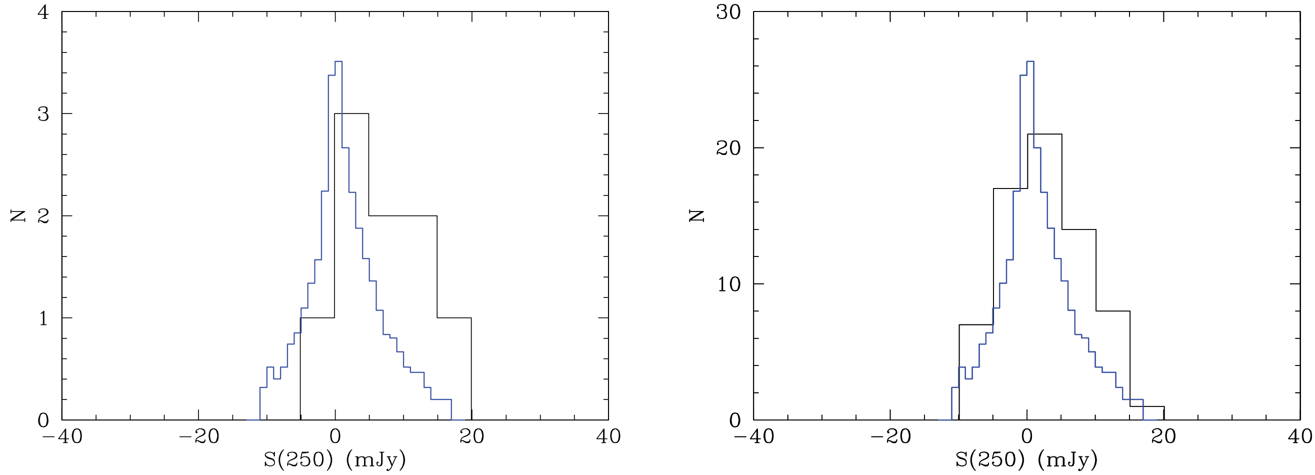

Figure 1. Histograms showing the 250 μm flux density distributions for LBGs (left) and BX/BMs (right). The blue curves show the flux density distribution in the entire GOODS-N field (control sample). In each case the control sample has been normalized by a factor equal to the total number of objects in each case ($N = 9$ for LBGs, $N = 69$ for BX/BM) divided by the total number of pixels in the whole GOODS-N image.

continuum. Thus, the MIPS-detected LBGs (with the strongest 6 μm continuum) are likely to be amongst the most luminous $z \sim 3$ LBGs. For $z \sim 2$ BX/BMs the MIPS 24 μm band includes contributions from both the 7.7 μm PAH feature and the underlying continuum. However, $z \sim 2$ galaxy populations show a wide variety in their $L_{5\text{–}8.5\,\mu\text{m}}$ rest-frame luminosity, with BX/BMs, in particular showing a relatively weak MIR continuum (Reddy et al. 2006). PAHs in BX/BMs might be intrinsically weak since metallicity is known to affect their strength (Houck et al. 2005). The combination of low MIR continuum plus weaker PAH features may be responsible for the low detection rate in the submm of 24 μm selected BX/BMs. We thus conclude that $z \sim 3$ LBGs detected by MIPS are likely to be on average more luminous than the MIPS-detected $z \sim 2$ BX/BMs.

2.3 Individual detections

In the previous section we examined the average submm properties of LBGs and BX/BMs. Here we take a closer look at individual detections, focusing on objects with MIPS detections . As discussed in Section 2.1 of the 69 MIPS–BX/BM objects, three are detected with $S_{250} > 20$ mJy and S/N > 3; however, two of those, BX1296 and BX1223, lie close (within ≤3 arcsec) to bright submm galaxies, BX1296 to GN07 and BX1223 to GN06 (the notation is from Pope et al. 2005). These confused cases have not been considered in this Letter. BM1326 is clearly detected, with $S_{250} = 22 \pm 5$ mJy while a further three BX/BMs appear in the 250 SPIRE map (and prior-based catalogue) but with 250 μm flux densities <10 mJy. Additionally, two (of the nine) LBGs, HDFN-M18 and HDFN-M23, appear to be present in the maps (and prior-based catalogue) although with fluxes below the 10 mJy level. We note that HDFN-M23 is included in the 5σ radio catalogue of Morrison et al. (2010), with a flux density of 21.2 ± 4 μJy.

3 RESULTS

3.1 Spectral energy distributions of LBGs

Fig. 2 shows the average spectral energy distribution (SED) of MIPS-detected LBGs and BX/BM galaxies. The SEDs have been constructed using available 'averaged' *UGRViJK*, IRAC, MIPS and SPIRE flux measurements. For the MIPS–LBGS we also use the 1.1 mm Aztec measurement from Magdis et al. (2010b). We fit the optical/near-IR part with model SEDs generated using the Bruzual & Charlot (2003, hereafter BC03) code, while the MIR-to-FIR part is fitted using Chary & Elbaz (2001, hereafter CE01) template SEDs. In brief, we use BC03 and construct stellar population models with a Salpeter IMF and constant SFR, which has been shown (van Dokkum et al. 2004; Rigopoulou et al. 2006) to provide an adequate description of the properties of high-redshift galaxies with ongoing star formation. Age, stellar mass, dust reddening $E(B - V)$ and SFRs are then derived from the model fits. It is beyond the scope of the present work to discuss these results; a detailed analysis of the properties of the stellar population in *Spitzer*-detected LBGs can be found in e.g. Rigopoulou et al. (2006), Magdis et al. (2010a, for LBGs) and Reddy et al. (2006, for BX/BMs). It is however worth noting the differences in the optical part of the SED with the BX/BM galaxies showing a much 'bluer' SED.

We fit the FIR/submm part with templates from the CE01 library, with the best-fitting templates rendering mean $\langle L_{\rm IR} \rangle$ values of $2.8(\pm 0.6) \times 10^{12}$ $\mathrm{L}_\odot$ for MIPS–LBGS and $1.5(\pm 0.5) \times 10^{11}$ $\mathrm{L}_\odot$ for MIPS–BX/BMs. The derived averaged $L_{\rm IR}$ for LBGs is typical of those seen in ultraluminous infrared galaxies (ULIRGs). Using the IR luminosities we derive average star formation rates ⟨SFRs⟩ of 296 and 245 $\mathrm{M}_\odot\,\mathrm{yr}^{-1}$, for the $z \sim 3$ LBGs and BX/BM galaxies, respectively. The ⟨SFR⟩ derived from the IR for LBGs is in agreement with the radio SFR estimate (280 ± 85 $\mathrm{M}_\odot\,\mathrm{yr}^{-1}$) but higher than the UV SFR estimate (250^{+35}_{-80} $\mathrm{M}_\odot\,\mathrm{yr}^{-1}$) reported in Magdis et al. (2010b). Turning to the BX/BM galaxies, the present SFR estimates agree well with those derived from the UV (Reddy et al. 2006) for *UGR*-selected galaxies.

3.2 Dust, temperature and mass

To derive the dust temperature, we use a single-temperature greybody fitting function (Hildebrand 1983) in which the thermal dust spectrum is approximated by $F_\nu = Q_\nu B_\nu(T_{\rm d})$, where B_ν is the Planck function, $Q_\nu = Q_0(\nu/\nu_0)^{\beta_{\rm d}}$ is the dust emissivity (with $1 \le \beta_{\rm d} \le 2$) and $T_{\rm d}$ is the effective dust temperature. For $h\nu/kT_{\rm d} \ge 1$ the spectrum becomes

$$F_\nu \propto \frac{\nu^{3+\beta_{\rm d}}}{\exp(h\nu/kT_{\rm d}) - 1}. \tag{1}$$

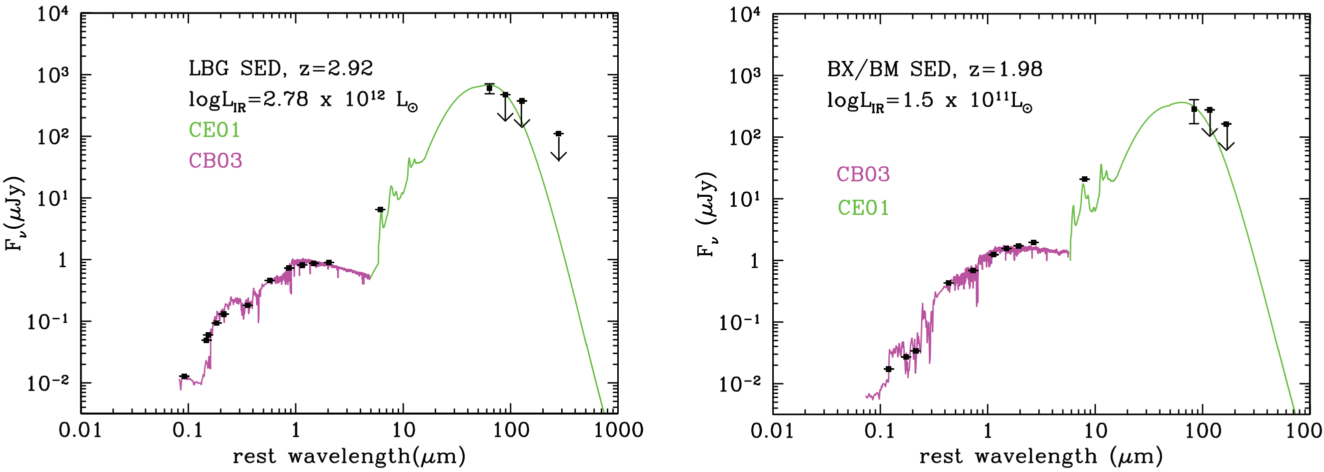

Figure 2. Rest-frame average SED of MIPS-detected LBGs (left) and $1 < z < 2.5$ BX/BMs (right) galaxies. For the SEDs we used mean values of *UGRViJK*, IRAC, MIPS, the mean value derived from SPIRE 250 μm and upper limits from SPIRE 350, 500 μm and Aztec 1.1 mm measurements (for $z \sim 3$ LBGs only). The rest-frame UV/optical is fitted with BC03 models (magenta) while the mid-infrared/far-infrared part of the SED is fitted with CE01 templates (green line).

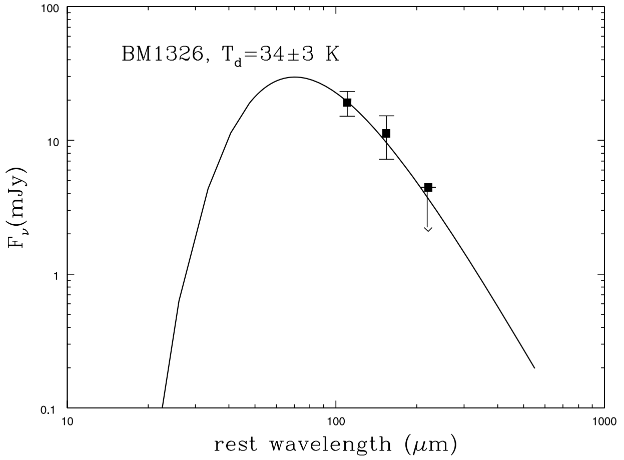

Figure 3. Modified blackbody temperature fit for the galaxy BM1326 (which is individually detected at the SPIRE bands). The black filled squares represent the individual detections at 250, 350 and 500 µm. For the fit we have fixed $\beta_d = 1.5$.

Since T_d and β_d are degenerate for sparsely sampled SEDs we have fixed $\beta_d = 1.5$ (e.g. Blain, Barnard & Chapman 2003) which is consistent with SED fitting of low and high-z systems (e.g. Dunne et al. 2001). A higher value of β_d will result in lower dust temperatures (Sajina et al. 2006). The dust temperature for BM1326 was obtained from the best-fitting model derived from minimization of the χ^2 values (Fig. 3) . The uncertainty in the measurement was obtained by repeating the procedure based on perturbed values of the photometric points within their errors.

To derive dust masses we follow

$$M_d = \frac{S_\nu D_L^2}{\kappa(\lambda_{\rm rest}) B_\nu(\lambda_{\rm rest}, T_d)}, \qquad (2)$$

where M_d is the total dust mass, S_ν is the observed flux density, D_L is luminosity distance, $\kappa(\lambda_{\rm rest})$ is the rest frame dust mass absorption coefficient (taken from Weingartner & Draine 2001) and $B_\nu(\lambda_{\rm rest}, T_d)$ is the Planck function. For the $z \sim 3$ LBGs we assume T_d = 45 K, a value chosen from T_d estimates for local ULIRGs (Lisenfeld, Isaak & Hills 2009) since the average MIPS–LBG appears to have $L_{\rm IR} > 10^{12}$ $L_\odot$. We derive dust masses of $M_d = 5.5 \pm 1.6 \times 10^8$ $M_\odot$ and $M_d = 12.8 \pm 2.3 \times 10^8$ $M_\odot$ for the LBGs and for BM1326, respectively.

4 DUST OBSCURATION IN UV-SELECTED GALAXIES

The present SPIRE observations allow us to probe the cold dust peak of LBGs, determine their FIR luminosity, dust temperature and dust mass from the FIR alone with minimal additional assumptions. Earlier attempts to detect submm emission from LBGs [with targets selected mostly based on SFR(UV) estimates] were not met with success (e.g. Chapman et al. 2000; Peacock et al. 2000). These initial results led to suggestions that either T_d is high ($T_d \geq 90$ K) or, that estimates of $L_{\rm IR}$ from the rest-frame UV and/or from the scatter in the UV-slope/FIR relation are uncertain (e.g. Chapman et al. 2000). Recently, Rigopoulou et al. (2010) reported 1.2 mm detections of two LBGs in the Extended Groth Strip (EGS), both are detected in the MIPS 24 µm imaging survey of the EGS (for the full SEDs see Rigopoulou et al. 2006). Briefly, their properties are similar to those of the GOODS-N $z \sim 3$ LBGs with S_{24} in the 50–100 µJy range. Using CE01 models we infer IR luminosities, $L_{\rm IR} \sim$ few × 10^{12} $L_\odot$ for each of these LBGs.

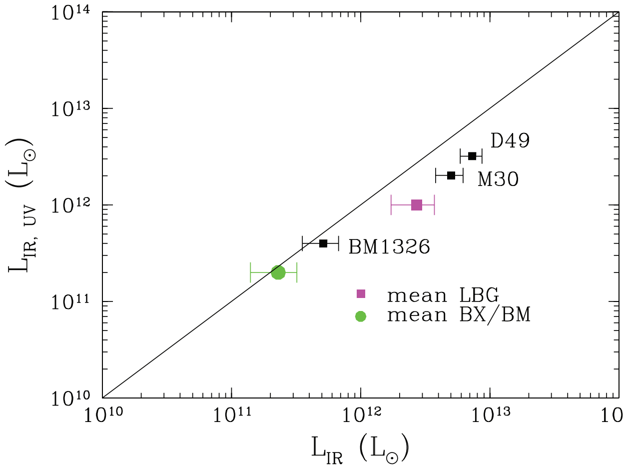

Figure 4. A comparison of estimates of $L_{\rm IR}$ from the present submm observations and from the UV ($L_{\rm IR,UV}$) for the average $z \sim 3$ LBGs (magenta), the average $z \sim 2$ BX/BMs (green), together with the BM1326 and D49 and M30 (the two LBGs with 1.2 mm detections). The solid line represents the $L_{\rm IR,UV} \sim L_{\rm IR}$.

Let us now focus on the MIPS-detected LBGs and BX/BMs using the mean LBG properties reported in Section 3.1 and compare $L_{\rm IR}$ values from the SPIRE data to those derived from the UV. $L_{\rm IR,UV}$ is determined as follows: at $z \sim 3$, G and R bands correspond to rest-frame 1200 and 1500 Å, respectively, thus allowing us to estimate the slope β. Assuming solar metallicity, Salpeter IMF and continuous dust-free star formation models we use the BC03 code to generate SEDs to fit each of the LBGs, assuming the Calzetti et al. (2000) attenuation law (but see also Buat et al. 2010 for a discussion of alternative extinction laws). Based on the best-fitting model we derive extinction values $E(B - V)$ and infer the observed and intrinsic 1500 Å flux density and subsequently, L_{1500} luminosity. We repeat the same process for the two galaxies with mm detections and the $z \sim 2$ mean BX/BM galaxies (using the B-band flux density to estimate the intrinsic L_{1500} luminosity).

The results are plotted in Fig. 4. The UV appears to underestimate the $L_{\rm IR,UV}$ of both the averaged $z \sim 3$ LBG (and the two LBGs with additional mm detections) by a factor of ∼2. This is perhaps not surprising given that the LBGs that appear to be detected in the submm regime are all ULIRGs. It is known that the UV underpredicts the $L_{\rm IR}$ for both local ULIRGs (e.g. Howell et al. 2010) and $z > 2$ submm-luminous galaxies. On the other hand, it appears that the UV provides a better estimate (closer to the measured $L_{\rm IR}$) for the averaged BX/BMs.

Finally, it is instructive to look at variations of the obscuration of these UV-selected galaxies. For this purpose we examine the bolometric luminosity (defined as the sum of the IR and UV luminosities) as a function of obscuration (approximated by the ratio of IR-to-UV luminosity) for LBGs and BX/BMs. For comparison we include submm-luminous and *UGR*-selected $z \sim 2$ galaxies (from Reddy et al. 2006, and references therein). The resulting plot is shown in Fig. 5. The straight line indicates the correlation found by Reddy et al. (2006, 2010) for $z \sim 2$ *UGR*-selected galaxies. The averaged $z \sim 3$ LBG and the two individually detected ones appear to follow the relation defined for the $z \sim 2$ galaxies. In terms of luminosities, both averaged LBGs and BX/BMs have similar $L_{\rm UV}$ (few × 10^{10} $L_\odot$) but LBGs have higher $L_{\rm IR}$ and thus higher $L_{\rm FIR}/L_{\rm UV}$

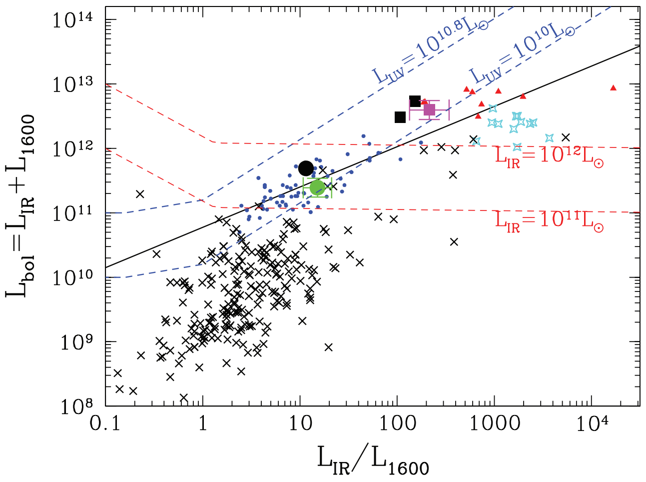

Figure 5. Bolometric luminosity, approximated as the sum of the IR and UV luminosities, versus IR-to-UV luminosity ratio (dust obscuration). Small blue circles are z ∼2 spectroscopically confirmed BX/BMs (from Reddy et al. 2006), red triangles represent submm-luminous galaxies, black crosses are local normal (Bell et al. 2003) and starburst (Brandl et al. 2006) galaxies and cyan stars are ULIRGs. The large black circle corresponds to BM1326 while the large green circle is the average BX/BM. Magenta and black squares are the average LBGs and the two LBGs with mm detections. The solid line indicates the best-fitting linear relation for spectroscopically confirmed *UGR*-galaxies detected at 24 μm (from Reddy et al. 2006). The red and blue dashed lines are lines of constant L_{UV} and L_{IR} luminosity. The error bars for the stacked LBG (magenta) and BX/BM (green) values have been magnified for clarity.

ratio. Since it is well established that obscuration decreases with increasing redshift (Reddy et al. 2006, 2010; Adelberger & Steidel 2000), the difference in the L_{FIR}/L_{UV} ratio must be attributed to different causes. While selection effects are likely to play a role (see Section 2.2) we argue that possible differences in morphologies, dust distribution and extent of star-forming regions are also likely to contribute. Morphological studies of UV-selected $z \sim 2$ and $z \sim 3$ galaxies in the GOODS-N field find few differences between the two samples (Law et al. 2007), although dustier galaxies [as evidenced by E(B-V)] were found to show more nebulous UV morphologies. Finally, since MIPS-detected LBGs have ULIRG-like luminosities (Section 3.1) it is possible that their UV and IR emissions originate in different regions (as observed in local ULIRGs, e.g. Wang et al. 2004, see also Huang et al. 2007) and thus could account for the higher L_{IR}/L_{UV} ratio observed.

ACKNOWLEDGMENTS

SPIRE has been developed by a consortium of institutes led by Cardiff University (UK) and including University of Lethbridge (Canada); NAOC (China); CEA, LAM (France); IFSI, University of Padua (Italy); IAC (Spain); Stockholm Observatory (Sweden); Imperial College London, RAL, UCL-MSSL, UKATC, University of Sussex (UK); Caltech, JPL, NHSC, University of Colorado (USA). This development has been supported by national funding agencies: CSA (Canada); NAOC (China); CEA, CNES, CNRS (France); ASI (Italy); MCINN (Spain); SNSB (Sweden); STFC (UK) and NASA (USA). The data presented in this Letter will be released through the *Herschel* data base in Marseille HeDaM (hedam.oamp.fr/HerMES).

REFERENCES

Adelberger K. L., Steidel C. C., 2000, ApJ, 544, 218
Bell E. F., McIntosh D. H., Katz N., Weinberg M. D., 2003, ApJS, 149, 289
Blain A. W., Barnard V. E., Chapman S. C., 2003, MNRAS, 338, 753
Brand B. R. et al., 2006, ApJ, 653, 1127
Buat V. et al., 2010, MNRAS, in press
Bruzual G., Charlot S., 2003, MNRAS, 344, 1000 (BC03)
Calzetti D., Armus L., Bohlin R. G., Kinney A. L., Koornneef S., Storchi-Bergmann T., 2000, ApJ, 533, 628
Chapman S. C., Casey C. C., 2009, MNRAS, 398, 1615
Chapman S. C. et al., 2000, MNRAS, 319, 318
Chary R.-R., Elbaz D., 2001, ApJ, 556, 562 (CE01)
Dunne L. et al., 2001, MNRAS, 327, 697
Griffin M. J. et al., 2010, A&A, 518, 3
Hildebrand R. H. et al., 1983, Quart. J. Roy. Astron. Soc., 24, 267
Houck J. R. et al., 2005, ApJ, 622, 105
Howell J. H. et al., 2010, ApJ, 715, 572
Huang J.-S. et al., 2005, ApJ, 634, 137
Huang, J.-S. et al., 2007, ApJ, 660, L69
Law D. R. et al., 2007, ApJ, 656, 1
Lisenfeld U., Isaak K. G., Hills R., 2000, MNRAS, 312, 433
Magdis G. et al., 2008, MNRAS, 386, 11
Magdis G., Rigopoulou D., Huang J.-S., Fazio G. G., 2010a, MNRAS, 401, 521
Magdis G. et al., 2010b, ApJ, 714, 1740
Marsden G. et al., 2009, ApJ, 707, 1729
Morrison G. E. et al., 2010, ApJS, 188, 178
Nguyen H. T. et al., 2010, A&A, 518, 5
Oliver S. J. et al., 2010, A&A, 518, 21
Peacock J. et al., 2000, MNRAS, 318, 535
Pilbratt G. et al., 2010, A&A, 518, 1
Pope A., Borys C., Scott D., Conselice C., Dickinson M., Mobasher B., 2005, MNRAS, 358, 149
Reddy N., Steidel C. C., 2009, ApJ, 692, 778
Reddy N. A. et al., 2006, ApJ, 644, 792
Reddy N. A. et al., 2010, ApJ, 712, 1070
Rigopoulou D. et al., 2006, ApJ, 648, 81
Rigopoulou D. et al., 2010, MNRAS, submitted
Roseboom I. et al., 2010, MNRAS, in press
Sajina A. et al., 2006, MNRAS, 269, 939
Steidel C. C., Adelberger K. L., Giavalisco M., Dickinson M., Pettini M., 1999, ApJ, 519, 1
Steidel C. C., Adelberger K. L., Shapey A. E., Dickinson M., Pettini M., Giavalisco M., 2003, ApJ, 592, 728
Steidel C. C., Hamilton D., 1993, AJ, 105, 2017
Swinyard B. M. et al., 2010, A&A, 518, 4
van Dokkum P. G. et al., 2004, ApJ, 611, 703
Weingartner J. C., Draine B. T., 2001, ApJ, 548, 296